Structural Engineering and Mechanics, Vol. 4, No. 6 (1996) 679-702
DOI: http://dx.doi.org/10.12989/sem.1996.4.6.679

Numerical analysis of plasma-sprayed ceramic coatings for high-temperature applications

Ioannis St. Doltsinis†, Kai-Uwe Haller‡ and Rainer Handel‡

Institute for Computer Applications, University of Stuttgart, Stuttgart, Germany

Abstract. The finite element method is employed in conjunction with micromechanical modelling in order to assess the performance of ceramic thermal barrier coatings applied to structural components. The study comprises the conditions of the deposition of the coating by plasma spraying as well as the thermal cycling of the coated component, and it addresses particularly turbine blades. They are exposed to high temperature changes strongly influencing the behaviour of the core material and inducing damage in the ceramic material by intense straining. A concept of failure analysis is discussed starting from distributed microcracking in the ceramic material, progressing to the formation of macroscopic crack patterns and examining their potential for propagation across the coating. The theory is in good agreement with experimental observations, and may therefore be utilized in proposing improvements for a delayed initiation of failure, thus increasing the lifetime of components with ceramic thermal barrier coatings.

Key words: ceramic thermal barrier coatings; finite element analysis; brittle microcracking model; fracture mechanics.

1. Introduction

Technological progress in heat engine systems is driven by the necessity of increasing efficiency in compliance with environmental protection. This requires structural components to be operated at temperatures higher than the material is able to sustain without substantial deterioration of its mechanical properties. Therefore thermal barrier coatings (TBC) are applied to surfaces exposed to elevated temperatures, protecting the structural part from the high temperature and/or an aggresive medium at operation. Ceramic coatings made of yttria-stabilized zirconia are well established as thermal barriers and are conveniently produced by plasma spraying. Thereby, the coating layer is formed by the impingement of small molten particles on the structural part to be coated. The coating material is injected in powder form into a plasma torch of approximately 20 000 K, is melted and deposited by the jet. For a description of this manufacturing process the reader is referred to the pertinent literature (for instance Zaat 1983).

The state of the art of plasma sprayed thermal barrier coatings leaves space for improving their performance. In the present study, numerical models are developed for the thermal and mechanical analysis of thermal barrier coatings applied to structural components. Modelling encompasses the consequences of manufacturing the coating, the thermal cycling under testing or service conditions, and the initiation and potential of failure. The finite element method

† Project Leader
‡ Research Fellow

is employed as a tool for the discretized representation of the problem on the computer. It had to be combined to a description of damage by distributed microcracking of the ceramic coating material.

The conditions during application of the ceramic coating influence its performance under thermal cycling. In plasma-spraying, the molten powder material splats on the substrate. Rapid solidification and cooling-down to substrate temperature, the quenching of locally deposited material, may leave appreciable long-range stresses, and determines also the microstructure and the macroscopic properties of the coating. Residual stresses are commonly considered as the result of cooling-down to ambient temperature of the component after deposition. The process is of interest since it may induce damage in the coating material by microcracking, thus influencing local elastic properties beyond quenching. On the other hand, residual stresses do not appropriately reflect the effect of the manufacturing conditions during thermal cycling if the core material is highly temperature sensitive in the range of operation. Then rather the thermal conditions at the state from which stress-inducing strains develop appear relevant.

Computer simulations of thermal cycling tests on turbine blades provide detailed information on the nature of strain and stress, their distribution and intensity as a function of time. Thereby critical locations can be identified in the coating and were confirmed by experimentalists to be prone to failure. In addition, numerical analysis indicates the reversals from heating to cooling in the cycle as critical instants inducing a cooling-shock in the blade coating. The high cycling stresses induce cracking on the microscopic level in the ceramic coating and thus affect its macroscopic mechanical properties. In order to account for this phenomenon, a numerical model was developed with reference to an elastic continuum containing cracks (Kachanov 1987). The approach is applied here in conjunction with the topology of the coating microstructure which defines a network of potential cracks along grain boundaries. On this basis, the proposed model (Doltsinis, *et al.* 1992) describes the evolution of crack patterns, under the action of macroscopic stress or strain and short-range microscopic strains left from deposition. The micromechanics model indicates the possible appearance of localized crack patterns which may propagate as macroscopic cracks across the coating layer. Fracture mechanics analysis, then assesses the potential for crack extension at critical locations in the coating. The computation confirms that energy dissipation by distributed microcracking substantially reduces the potential for macroscopic crack extension. The predictions based on the numerical modelling reasonably interpret observations in the testing laboratory. The knowledge evolving from numerical computer simulation appears useful in proposing modifications for the manufacturing and the operation of the coating in order to delay failure, thus increasing lifetime.

2. Thermoelastic analysis

Transient thermal and elastic analysis by the finite element method may be regarded a standard procedure. It is briefly recalled in the following for an introduction of the notation used in the paper. In this connection, we consider a finite element representation of the problem, where transient mechanical states are governed at each instant t by the condition of quasistatic equilibrium in the form

$$\boldsymbol{S}(\sigma)=\boldsymbol{R}(t) \tag{1}$$

The column matrices (vectors) $\boldsymbol{S}$ and $\boldsymbol{R}$ refer to the N nodal points of the finite element system. The vector $\boldsymbol{R}$ comprises the force components at each nodal point equivalent of the externally applied loading. The vector $\boldsymbol{S}$ comprises the resultants at the nodal points of the internal stress σ. They are obtained from individual element contributions $\boldsymbol{S}_e$ by accumulation

$$\boldsymbol{S}=\{\boldsymbol{a}_e\}^t\{\boldsymbol{S}_e\} \text{ where } \boldsymbol{S}_e=\int_{V_e}\boldsymbol{a}^t\sigma dV \tag{2}$$

The symbolic operator $\{\boldsymbol{a}_e\}$ is known as the incidence matrix of the mesh, the matrix $\boldsymbol{a}$ denotes the small strain operator appertaining to the kinematics on the element level.

In thermoelasticity, the constitutive relation for the stress components in the vector array σ reads

$$\sigma=\kappa[\gamma-\eta] \tag{3}$$

Here κ denotes the material elasticity matrix, and the vector array

$$\gamma=\boldsymbol{a}\boldsymbol{U}_e \text{ with } \boldsymbol{U}_e=\boldsymbol{a}_e\boldsymbol{U} \tag{4}$$

defines the strain state as from the displacements $\boldsymbol{U}_e$ allocated to the element via $\boldsymbol{a}_e$. The vector $\boldsymbol{U}$ comprises the nodal point displacements of the finite element mesh with reference to the coordinate axes.

In the stress-strain relation Eq. (3), the vector array

$$\eta=(T-{}^\circ T)\,\alpha \tag{5}$$

represents the thermal strain determined with the coefficients of linear thermal expansion in α, the actual local temperature T and the reference temperature ${}^\circ T$ at the stress-free state. Isotropic thermal expansion is characterized by normal strain components associated to a single scalar coefficient α.

When the thermal state is given, Eq. (1) determines the displacements $\boldsymbol{U}$ and may be solved as by the instruction

$$\boldsymbol{U}_{i+1}=\boldsymbol{U}_i+\boldsymbol{K}_i^{-1}[\boldsymbol{R}-\boldsymbol{S}_i] \tag{6}$$

Eq. (6) extends over the unknowns of the nodal point displacements only. The indicated iteration refers to the nonlinear case where the elastic stiffness matrix $\boldsymbol{K}$ of the system depends on the solution. In linear problems, the first pass through Eq. (6) with $\boldsymbol{U}_0=\boldsymbol{0}$ operates on the applied forces cum the thermal constituent of the vector $\boldsymbol{S}$, and furnishes the solution $\boldsymbol{U}=\boldsymbol{U}_1$ at once.

The local temperature T entering Eq. (5) may be interpolated from the values at the element nodal points in the vector $\boldsymbol{T}_e$,

$$T=\bar{\omega}\boldsymbol{T}_e \text{ where } \boldsymbol{T}_e=\bar{\boldsymbol{a}}_e\boldsymbol{T} \tag{7}$$

and $\boldsymbol{T}$ denotes the vector array comprising the temperature values at the N mesh nodal points. Transient temperature fields are governed at each instant t by the time-dependent heat conduction equation. Its discretized form reads

$$\boldsymbol{C}\dot{\boldsymbol{T}}+\boldsymbol{L}\boldsymbol{T}=\dot{\boldsymbol{Q}} \tag{8}$$

and $\boldsymbol{C}$ denotes the heat capacity matrix, $\boldsymbol{L}$ the thermal conductivity matrix, the vector $\dot{\boldsymbol{Q}}$ comprises the thermal loading at the mesh nodal points. The superposed dot denotes as usually time

rates.

It might be recalled that Eq. (8) emanates from the local energy balance,

$$\dot{u}=\frac{1}{\rho}\,\sigma'\,\dot{\gamma}+\dot{q} \tag{9}$$

where u denotes the specific internal energy (per unit mass), ρ the density at the stress-free state where the stress σ and the strain γ are referred to, and the scalar product $\sigma'\dot{\gamma}$ provides the rate of mechanical work. The quantity $\dot{q}$ represents the rate of heat supply per unit mass, defined by

$$\dot{q}=-\frac{1}{\rho}\,\mathrm{div}\,\dot{\boldsymbol{q}}+\dot{q}_s \tag{10}$$

with the heat flow

$$\dot{\boldsymbol{q}}=-\lambda\ \mathrm{grad}\ T \tag{11}$$

as given by Fourier's law in conjunction with the heat conductivity λ of the material, and $\dot{q}_s$ the contribution of local heat sources.

The specific internal energy $u(\gamma, T)$ is considered a function of state defined by the variables γ, T. Therefore,

$$\dot{u}=\frac{\partial u}{\partial \gamma}\,\dot{\gamma}+\frac{\partial u}{\partial T}\,\dot{T} \tag{12}$$

in Eq. (9). Use of the second fundamental law of thermodynamics for $\dot{q}=T\dot{s}$ excluding any mechanical irreversibility, and of the notion of an entropy function $s(\gamma, T)$, leads to

$$\left.\frac{\partial u}{\partial \gamma}\right|_T=\frac{1}{\rho}\left[\sigma-T\frac{\partial \sigma}{\partial T}\right]', \quad \left.\frac{\partial \boldsymbol{u}}{\partial T}\right|_\gamma=T\left.\frac{\partial s}{\partial T}\right|_\gamma=\left.\frac{\partial q}{\partial T}\right|_\gamma=c_\gamma \tag{13}$$

and c_γ is the specific heat capacity at constant strain, $\dot{\gamma}=\mathbf{0}$.

Substitution of Eq. (13) in Eq. (12) and with Eqs. (10), (11), the energy balance Eq. (9) yields

$$\rho c_\gamma \dot{T}-T\frac{\partial \sigma'}{\partial T}\,\dot{\gamma}-\mathrm{div}(\lambda\ \mathrm{grad}\ T)=\rho\dot{q}_s \tag{14}$$

A comparison between Eq. (14) and its discretized counterpart Eq. (8) reveals that the matrix $\boldsymbol{L}$ not only reflects heat conduction, but also incorporates the thermomechanical coupling term present in Eq. (14). In addition, convective heat transfer at the rate $\alpha_c\,(T-T_\infty)$ via the surface also contributes to the matrix $\boldsymbol{L}$ of the system by the unknown term $\alpha_c T$ whilst $\alpha_c T_\infty$ from the ambient contributes to the thermal loading $\dot{\boldsymbol{Q}}$ on the right-hand side.

Following Eq. (14), the heat capacity matrix $\boldsymbol{C}$ refers to c_γ as obtained at $\dot{\gamma}=\mathbf{0}$. For solids, the specific heat capacity c measured at zero stress is normally provided instead. For a correlation of the alternatively defined specific heat capacities of the material, the strain rate $\dot{\gamma}$ in Eq. (12) may be expressed via the stress-strain relation Eq. (3). For constant material parameters Eq. (12) then becomes

$$\dot{u}=\frac{\partial u}{\partial \gamma}\kappa^{-1}\dot{\sigma}+\left[\frac{\partial u}{\partial \gamma}\alpha+\frac{\partial u}{\partial T}\right]\dot{T} \tag{15}$$

Comparing Eq. (9) with Eq. (15) for $\sigma=\mathbf{0}$ and $\dot{\sigma}=\mathbf{0}$ one may deduce the relationship

$$c=\frac{\partial q}{\partial T}\bigg|_{\sigma=0}=\frac{\partial u}{\partial \gamma}\alpha+c_\gamma \tag{16}$$

between the specific heat capacity c at zero stress and c_γ at constant strain, Eq. (13).

When the mechanical contribution to the thermal conductivity equation is either known or negligible, Eq. (8) may be solved in conjunction with an approximate integration scheme,

$$T={}^aT+(1-\zeta)\,\tau\,{}^a\dot{T}+\zeta\tau\dot{T} \tag{17}$$

advancing incrementally the temperature from the state at time $t={}^at$ to the state at time $t={}^at+\tau$, and $\mathbf{0}\leq\zeta\leq\mathbf{1}$ is the collocation parameter. The temperature rate required in Eq. (17) is obtained by solving Eq. (8) which may be nonlinear in the temperature. In analogy to Eq. (6),

$$\dot{\boldsymbol{T}}_{i+1}=\dot{\boldsymbol{T}}_i+[\boldsymbol{C}+\zeta\tau\boldsymbol{L}]^{-1}[\dot{\boldsymbol{Q}}-\boldsymbol{C}\dot{\boldsymbol{T}}-\boldsymbol{L}\boldsymbol{T}]_i \tag{18}$$

and the iteration matrix refers to an approximate linearization of the residuum with respect to the unknown $\dot{T}$. Explicit integration of the temperature ($\zeta=\mathbf{0}$) simplifies the solution making Eq. (18) a linear equation in $\dot{T}$, but accuracy and numerical stability are restricted. If Eq. (8) is coupled to Eq. (6) by the mechanical term in Eq. (14), the system of the two thermomechanical vector equations may be solved by an iterative exchange of partial solutions between the mechanical and the thermal subproblem (Doltsinis 1993).

3. Damage by microcracking

Characteristic to the ceramic material of the coating layer is the capability of the development of microcracks which alter the material response under thermal and/or mechanical loading. For a constitutive description of the damaging material, our model considers an elastic solid containing cracks, Fig. 1, and follows the development of their formation under the application of stress, with reference to the microstructure of the material.

In order to define the nature of the macroscopic stress-strain relations we consider a representative volume V of the material composed of an elastic matrix (volume V_M) containing a number

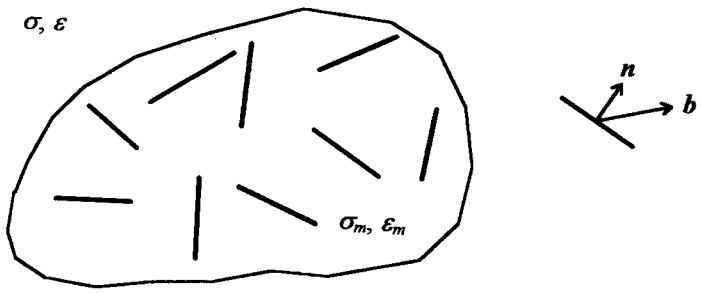

Fig. 1 Elastic solid containing cracks.

of cavities (volume V_C), and $V=V_M+V_C$. The remotely applied, macroscopic stress σ is specified by the average of the microscopic stresses σ_m in the volume

$$\langle\sigma_m\rangle V=\int_{V_M}\sigma_m dV+\int_{V_C}\sigma_m dV=\langle\sigma_M\rangle V_M+\mathbf{0} \tag{19}$$

and $\sigma=\langle\sigma_m\rangle$. Since the cavities are considered stress-free, the averaging process extends over the matrix only and yields $\langle\sigma_M\rangle$. Analogously, the microscopic elastic strain ε_m provides,

$$\langle\varepsilon_m\rangle V=\int_{V_M}\varepsilon_m dV+\int_{V_C}\varepsilon_m dV=\langle\varepsilon_M\rangle V_M+\langle\varepsilon_C\rangle V_C \tag{20}$$

and the macroscopic elastic strain reads $\varepsilon=\langle\varepsilon_m\rangle$. The quantities $\langle\varepsilon_M\rangle$ and $\langle\varepsilon_C\rangle$ in Eq. (20) denote the average over the matrix and the defects respectively. For the elastic matrix material,

$$\langle\varepsilon_M\rangle=\kappa_0^{-1}\langle\sigma_M\rangle \tag{21}$$

whilst the contribution of the cavities to the macroscopic strain is from the displacements along their boundaries.

Denoting the displacement vector along the cavity boundary by $\boldsymbol{u}$ and the external unit normal by $\boldsymbol{n}$, we may replace the strain integral over the cavities by,

$$\langle\varepsilon_C\rangle V_C=\int_{V_C}\varepsilon_m dV\leftarrow\frac{1}{2}\sum_{i=1}^{n}\int_{S_i}[\boldsymbol{u}\boldsymbol{n}^t+\boldsymbol{n}\boldsymbol{u}^t]\,dS \tag{22}$$

and integration in Eq. (22) extends over the surfaces S_i bounding the n cavities. The transition indicated in Eq. (22) implies also reduction to the presentation of the strain as a vector array. Let ε_C denote this ultimate result of the instruction of Eq. (22) normalized by the volume V. Then, we obtain from Eq. (20) with Eqs. (21), (19) for the macroscopic quantities

$$\varepsilon=\kappa_0^{-1}\sigma+\varepsilon_C \tag{23}$$

In order to establish a complete relation between the strain ε and the stress σ, the displacements $\boldsymbol{u}$ in Eq. (22) must be expressed in terms of the macroscopic stress σ. For the elastic solid with cracks under consideration, we adopt the procedure developed in (Kachanov 1987). For cracks in place of cavities, the surface integral in Eq. (22) may be evaluated along the one face only by replacing the displacement vector $\boldsymbol{u}$ by the vector $\boldsymbol{b}$ defining the displacement discontinuity across the crack (crack opening displacement). Flat cracks are characterized by unique normals $\boldsymbol{n}$, and defining an average $\langle\boldsymbol{b}\rangle$ over the area A of each crack we deduce the additional strain in Eq. (23) from the expression

$$\varepsilon_C\leftarrow\frac{1}{2V}\sum_{i=1}^{n}[\langle\boldsymbol{b}\rangle\boldsymbol{n}^t+\boldsymbol{n}\langle\boldsymbol{b}^t\rangle]_i A_i \tag{24}$$

The average crack opening displacement $\langle\boldsymbol{b}\rangle$ may be provided as a result of a traction vector $\boldsymbol{t}$ uniformly applied at the crack faces by the relation.

$$\langle\boldsymbol{b}\rangle=\boldsymbol{B}\boldsymbol{t} \tag{25}$$

The matrix $\boldsymbol{B}$, the crack compliance, depends on crack shape and size, the geometry of the sample and on the properties of the elastic medium. In the anisotropic case orientation is also

important. Expressions for representative crack geometries were given in (Kachanov 1987, 1992). For an illustration consider a rectilinear crack in the plane, and with reference to the n, s-system (normal and tangential to the crack line) Eq. (25) assumes the form

$$\begin{bmatrix} \langle b_n \rangle \\ \langle b_s \rangle \end{bmatrix} = \begin{bmatrix} B_{nn} & B_{ns} \\ B_{sn} & B_{ss} \end{bmatrix} \begin{bmatrix} t_n \\ t_s \end{bmatrix} \tag{26}$$

For the isotropic material normal and shear modes are uncoupled, and the off-diagonal terms in the matrix $\boldsymbol{B}$ vanish. Otherwise $B_{sn}=B_{ns}$ for the elastic medium and therefore $\boldsymbol{B}$ is a symmetric matrix. In the infinite plane, $B_{nn}=B_{ss}=\pi l/2E_0'$ (crack length l, $E_0'=$elastic modulus E_0 for plane stress, $E_0'=E_0/(1-\nu_0^2)$ for plane strain) and $B=(\pi l/2E_0')\,\boldsymbol{I}$(identity matrix $\boldsymbol{I}$) is an isotropic matrix invariant to coordinate rotations.

For a specification of the tractions entering Eq. (25), loading the linear elastic solid containing n cracks by the remote stress σ is considered equivalent to simultaneously loading the n crack faces by tractions $\sigma^t \boldsymbol{n}_i$ with σ denoting here matrix representation of the stress tensor. In order to comply with the assumptions of Eq. (25), however, this problem is substituted by n individual problems regarding each single crack isolated. Here, the traction is not known a priori since in addition to the remotely applied stress σ, the interaction with the other cracks must be accounted for. Accordingly, the traction at the ith crack may be represented as,

$$\boldsymbol{t}_i=[\sigma+\sum_{j\neq i}\sigma_{ij}]^t \boldsymbol{n}_i \tag{27}$$

and σ_{ij} denotes the stress distribution along the ith crack face induced by the traction acting on the jth crack face. With the simplifying assumption that the stress induced by the uniform (average) part of the respective tractions yields an accurate approximation, Eq. (27) may be transformed to a system determining the n average tractions $\langle \boldsymbol{t}_i \rangle$. This will be exemplified for the two-dimensional case in the following.

In the two-dimensional case, the crack-induced stress σ_j may be represented as

$$\sigma_j=p_j\sigma_{pj}+q_j\sigma_{qj} \tag{28}$$

where

$$p_j=\boldsymbol{n}_j^t\langle \boldsymbol{t}_j \rangle,\quad q_j=\boldsymbol{s}_j^t\langle \boldsymbol{t}_j \rangle \tag{29}$$

denote the average traction components along the normal direction $\boldsymbol{n}$ and the tangential direction $\boldsymbol{s}$ of the jth crack. The stress fields σ_{pj}, σ_{qj} are those arising in the elastic plane from unit uniform normal and shear tractions $p_j=1$ and $q_j=1$ respectively at the jth crack. Averaging Eq. (27) for the ith crack line and forming normal and tangential components as by Eq. (29), we obtain

$$p_i=p_{i0}+\sum_{j\neq i}(K_{ij}p_j+L_{ij}q_j),\qquad q_i=q_{i0}+\sum_{j\neq i}(M_{ij}p_j+N_{ij}q_j) \tag{30}$$

Here, the terms

$$p_{i0}=\boldsymbol{n}_i^t\sigma^t\boldsymbol{n}_i,\qquad q_{i0}=\boldsymbol{s}_i^t\sigma^t\boldsymbol{n}_i \tag{31}$$

refer to the traction along the ith line for the uncracked medium, and the coefficients of p_j, q_j in the sum may be identified as

$$K_{ij}=\boldsymbol{n}_i^t\left(\frac{1}{l_i}\int_i\sigma_{pj}^t\,dl\right)\boldsymbol{n}_i,\qquad L_{ij}=\boldsymbol{n}_i^t\left(\frac{1}{l_i}\int_i\sigma_{qj}^t\,dl\right)\boldsymbol{n}_i$$
$$M_{ij}=\boldsymbol{s}_i^t\left(\frac{1}{l_i}\int_i\sigma_{pj}^t\,dl\right)\boldsymbol{n}_i,\qquad N_{ij}=\boldsymbol{s}_i^t\left(\frac{1}{l_i}\int_i\sigma_{qj}^t\,dl\right)\boldsymbol{n}_i \tag{32}$$

They essentially require averaging of the elementary stress functions σ_{pj}, σ_{qj} over the length l_i of the ith crack.

Defining the $n\times 2$ vector array of the unknown tractions

$$P=\{p_1q_1p_2q_2\ \cdots\ p_nq_n\}$$

and

$$P_0=\{p_{10}q_{10}p_{20}q_{20}\ \cdots\ p_{n0}q_{n0}\} \tag{33}$$

for the projections of the applied stress, the matrix form of Eq. (30) reads

$$[\boldsymbol{I}-\boldsymbol{N}]\,\boldsymbol{P}=\boldsymbol{P}_0 \tag{34}$$

Eq. (34) may be solved for the unknown tractions in the vector $\boldsymbol{P}$ once the matrix $\boldsymbol{N}$ comprising the interaction coefficients from Eq. (32) is formed.

In the vector array $\boldsymbol{P}$, the entities p and q denote average traction components normal and tangential to the individual crack lines. The problem may instead be solved directly for the cartesian components. With Eq. (29) in Eq. (28), the average traction for the ith crack from Eq. (27) assumes the form

$$\langle\boldsymbol{t}_i\rangle=\sigma^t\boldsymbol{n}_i+\sum_{j\neq i}\boldsymbol{\Lambda}_{ij}\langle\boldsymbol{t}_j\rangle \tag{35}$$

In Eq. (35) the 2×2 matrix

$$\boldsymbol{\Lambda}_{ij}=\frac{1}{l_i}\int_i[\sigma_{pj}^t\boldsymbol{n}_i\boldsymbol{n}_j^t+\sigma_{qj}^t\boldsymbol{n}_i\boldsymbol{s}_j^t]\,dl \tag{36}$$

defines the average traction induced at the ith crack because of the presence of the jth crack in the elastic plane. Extension of Eq. (35) to all n cracks supplies the matrix equation

$$[\boldsymbol{I}-[\boldsymbol{\Lambda}_{ij}]]\,\{\langle\boldsymbol{t}_i\rangle\}=\{\sigma^t\boldsymbol{n}_i\} \tag{37}$$

which may be solved for the unknowns $\langle\boldsymbol{t}_i\rangle$. In Eq. (37) the submatrix $\boldsymbol{\Lambda}_{ij}$ is zero for $i=j$. The constitutive description of the elastic solid with a defined crack system is now completed. For an applied stress σ Eq. (37) is solved for the tractions $\langle\boldsymbol{t}_i\rangle$ and then Eq. (25) provides the crack opening displacements $\langle\boldsymbol{b}_i\rangle$. The latter enter Eq. (24) for ε_C, the crack induced part of the strain in Eq. (23). Conversely, an inversion procedure yields the stress σ associated to a prescribed strain ε.

For a simulation of microcracking in the material, a sample representative of the structure is considered and provides a network of potential cracks along the grain boundaries. Information on the grain structure is therefore essential and must be available in a form suitable for numerical processing. To this purpose, artificial microstructures with specific characteristics are generated by a computer algorithm. In two dimensions, the procedure starts from a regular hexagonal lattice. The cells, representing grains, may be subject to a statistical distortion. A significant feature of plasma sprayed ceramic coatings is the lamellar structure introduced by the production process. In the model, lamellae are defined within the existing grain network by curves to which

neighbour triple points are displaced. Lattice distortion leads to only moderate fluctuations in grain size, and in order to obtain larger variations several adjacent grains are merged together. Columnar grains encountered perpendicular to the lamellae are modelled as well. Also, pores may be introduced by activating a graphical void growth process at randomly selected triple points in the sample. Fig. 2 reproduces a generated microstructure representative of the ceramic coating in subsequent applications.

Towards the dynamics of a microcracking network the constitutive description for the elastic solid with cracks is combined to a criterion for the separation of grain boundaries. In this connection, it is assumed that a facet of length l_i fails and forms a crack of the same length as soon as the energy $\int G_i dl_i$ released by this transition exceeds the surface energy $2\gamma l_i$ required for the separation of the material. With reference to a single crack in an infinite plane,

$$\int_i G(p_i)\, dl_i = \frac{\pi l_i^2 p_i^2}{4E_0'} \tag{38}$$

In Eq. (38), l_i denotes the length of the ith facet, and p_i the (tensile) traction normal to the facet, E_0' equals the elastic modulus E_0 of the matrix material for plane stress or $E_0/(1-\nu_0^2)$ for plane strain. The expression in Eq. (38) reflects integration of the energy release rate $G(p_i) = \pi l_i p_i / 2E_0'$ for the crack formation $0 \rightarrow l_i$. The same result may be alternatively obtained by determining for the crack length l_i the work of the traction p_i on the average crack opening displacement $\langle b_i \rangle = \pi l_i p_i / 2E_0'$.

Although the matrix material is considered elastically isotropic in the large, anisotropy of the individual grains contributes to the development of microscopic stress from cooling-down (Davidge *et al.* 1983). In this connection the effect of different grain orientations is accounted for by an anisotropy coefficient $0 \leq a \leq 1$ assigned to grain boundaries by a random distribution. The elastic energy rate $G(a_i)$ released during crack extension due to local anisotropy in conjunction with the homogeneous thermal strain η experienced by the material in cooling-down may be approximated by a relation proposed in (Buresch 1985). Its integration for $0 \rightarrow l_i$ furnishes

$$\int_i G(a_i)\, dl = \frac{E_0'\, \eta^2 a_i^2 l_i^2}{48} \tag{39}$$

For separation of the ith facet,

$$\int_i G_i dl_i = \int_i G(p_i)\, dl_i + \int_i G(a_i)\, dl_i \geq 2\gamma l_i \tag{40}$$

where the value of the specific surface energy γ is assumed lower along lamellae than between pores.

Crack formation may thus be pursued by the following instructions:

Loading loop

Define actual state of applied stress σ

Determine normal tractions $p_i(\sigma)$ at the $m \leq n$ facets

Facet loop

Determine critical $p_{i\,crit.}$ from $\frac{1}{l_i}\int_i G_i dl_i = 2\gamma$

Allocate a crack if $p_{i\,crit.} \leq p_i(\sigma)$

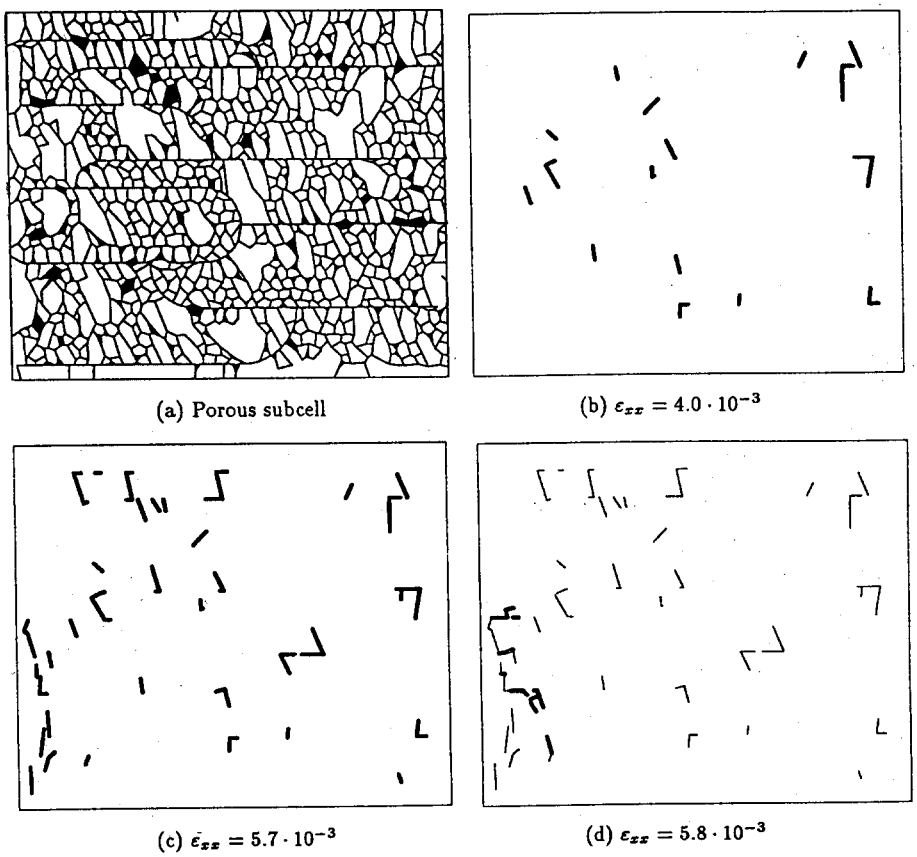

Fig. 2 Ceramic structure used for damage analysis. The lines are grain boundaries, the black areas pores. Under load, cracks indicated with black lines in the frames form and localize on the left-hand side of the sample.

End facets
Update facets (m) and cracks (n-m)
Determine elasticity matrix and strain state ε for actual crack pattern
End loading

In the procedure, already formed cracks induce tractions along the facets whilst facets do not contribute to the tractions along cracks. For monotonic loading, the intensity of the applied stress may be continuously adapted to each new forming crack as from $p_i(\sigma)=(p_{i\,crit.})$. Alternatively, it may be preferable to prescribe the strain state and to compute instead the associated stress. This is mandatory when the algorithm is combined to finite element analysis.

As an application of the microcracking algorithm, Fig. 2 demonstrates the development of crack patterns in an artificial sample. The rectangular sample has the dimensions 60 μm$\times$50 μm and is characterized by an average grain diameter of 1.5 μm, the specific surface energy $\gamma=2.0$ J/m^2 for grain facets whilst $\gamma=1.0$ J/m^2 along lamellae. In the original material $E=20$ Gpa, $\nu=0.15$. The loading consists of strains imposed along the horizontal and the vertical directions to the ratio $1/-\nu=1/-0.15$. Cracks start developing in rather diffuse patterns, localization at higher strains may be interpreted as macroscopic crack formation, cf. Fig. 2(c) and 2(d).

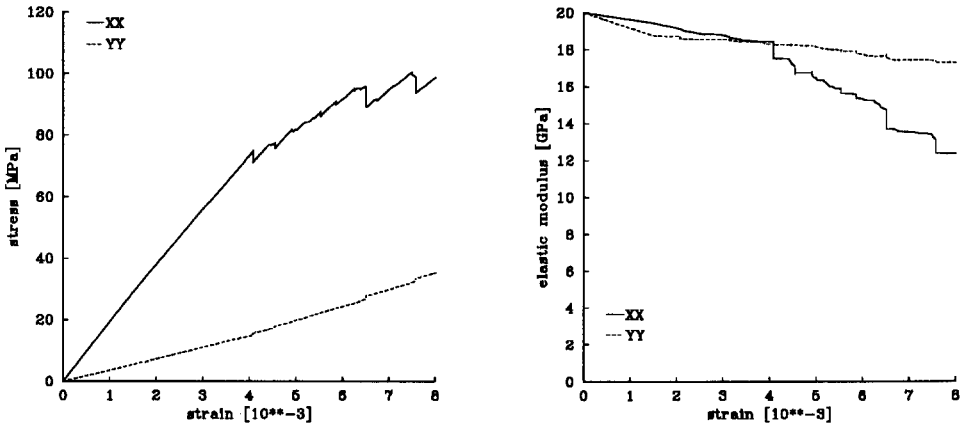

Fig. 3 Stress/strain diagram and elastic modulus for the ceramic coating.

Fig. 3 indicates the stress-strain behaviour along the axes of the rectangular, and provides information on the deterioration of the elasticity coefficients and the anisotropy induced by microcracking. The ratio between the strain components is here $1/-0.3$, but the results are practically the same as for the previous straining mode.

4. Fracture mechanics

The appearance of macroscopic crack patterns limits the applicability of the microcracking model and suggests an assessment of failure by the fracture mechanics approach. The energy release rate for crack extension under the actual loading conditions appears a suitable quantity for this purpose, and may be determined by a finite element representation of the system on the continuum level with the presence of cracks of macroscopic dimensions (Doltsinis 1979). Let in the finite element system, the area of an existing crack being virtually extended by the amount ∂A at constant boundary-, respectively loading conditions. The crack extension would change the displacements of the mesh nodal points by $\partial \boldsymbol{U}$ and the local strain by $\partial \gamma$. The associated energy variation of the loaded system is given by

$$\boldsymbol{R}^t \partial \boldsymbol{U} - \sum_{nel} \int_{V_e} \sigma^t \partial \gamma dV = G \partial A \tag{41}$$

and defines the energy release rate G. It is assumed that crack extension is effected by displacing the crack tip whilst the connectivity of the finite element mesh is maintained. Therefore the kinematic relations of Eq. (4) yield,

$$\partial \gamma = \boldsymbol{a}\, \partial \boldsymbol{U}_e + \partial \boldsymbol{a} \boldsymbol{U}_e \qquad \text{with} \qquad \partial \boldsymbol{U}_e = \boldsymbol{a}_e \partial \boldsymbol{U} \tag{42}$$

and $\partial \boldsymbol{a}$ is a consequence of the modified crack geometry. With Eq. (42), the element contributions in Eq. (41) become

$$\int_{V_e} \partial \gamma^t \sigma dV = \partial \boldsymbol{U}_e^t \int_{V_e} \boldsymbol{a}^t \sigma dV + \boldsymbol{U}_e^t \int_{V_e} \partial \boldsymbol{a}^t \sigma dV \tag{43}$$

and on account of Eq. (2)

$$\sum_{nel}\int_{V_e}\partial\gamma^t\sigma dV=\partial\boldsymbol{U}^t\boldsymbol{S}+\sum_{nel}\boldsymbol{U}_e^t\int_{V_e}\partial\boldsymbol{a}^t\sigma dV \tag{44}$$

Since the state is considered at equilibrium, cf. Eq. (1), the energy release is thus obtained from Eq. (41) as by

$$G\partial A=-\sum_{cel}\boldsymbol{U}_e^t\int_{V_e}\partial\boldsymbol{a}^t\sigma dV \tag{45}$$

In Eq. (45) the summation extends only over the elements involved in the modification of the crack geometry. Denoting the element stress resultants evaluated with the slightly modified geometry for the existing nodal point solution, by

$$[\boldsymbol{S}_e+\partial\boldsymbol{S}_e]=\int_{V_e}[\boldsymbol{a}+\partial\boldsymbol{a}]^t\sigma dV \tag{46}$$

we deduce from Eq. (45) the stability criterion for the crack as

$$G=-\frac{1}{\partial A}\sum_{cel}\boldsymbol{U}_e^t\partial\boldsymbol{S}_e\leq G_{crit.} \tag{47}$$

In Eq. (47), $G_{crit.}$ denotes the value of the energy release rate critical for the material.

For the determination of the energy release rate available for crack extension as by Eq. (47), the stress resultants at elements affected by the virtual displacement of the crack tip are calculated twice: for the original and the modified geometry, the difference yielding $\partial\boldsymbol{S}_e$. In this connection, the existing solution $\boldsymbol{U}_e$, $\boldsymbol{T}_e$ provides the stress σ, Eq. (3) with the respective element geometry in $\boldsymbol{a}$, Eq. (4), and $\bar{\omega}$, Eq. (7).

5. Computation tools and modelling of turbine blade

The Finite Element Programming System FEPS developed by the author s group at the ICA (Wüstenberg 1986) proves appropriate for the stress analysis regarding the application of the coating, and the thermal cycling of coated structural components (Doltsinis *et al.* 1995). The software system, designed ab initio for numerical computer simulations in research environments, is characterized by a flexibility for adaptation to specific requirements, and to various physical phenomena. Standard transient thermal and elastic analysis had to be tuned to the demands of modelling the production and thermal cycling of coated parts. In particular, the finite element algorithm was coupled to the numerical micromechanical model simulating damage of the ceramic material in the coating layer.

The computational and modelling tasks associated with the subject will be detailed for a turbine blade coated by a plasma-sprayed ceramic layer. Fig. 4 shows the cross-section of the turbine blade (20 mm span) and Fig. 5 a discretized model to which we will refer in the following. The finite element mesh was generated automatically from the geometrical data of the profile, and includes smoothing of the element size (Doltsinis 1990). A distinction has to be made between the blade material in the core (IN100), the 0.1 mm bond layer (Co-32%Ni-21%Cr-8%Al-Y) and

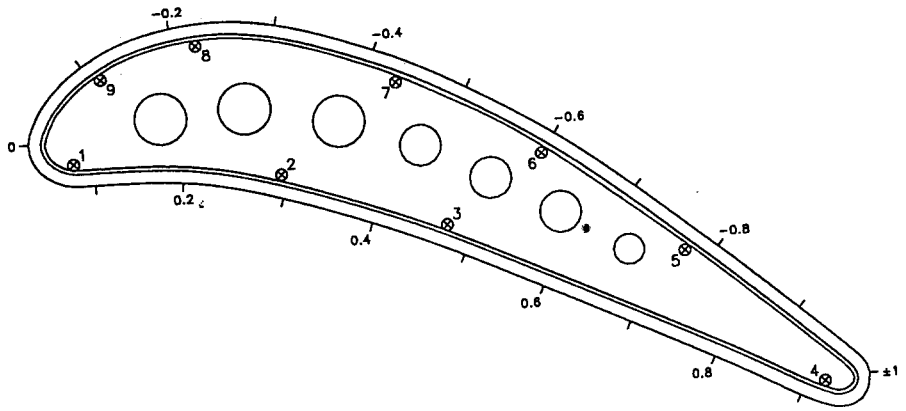

Fig. 4 Cross-section of the turbine blade. The outer two layers represent the ceramic coating and the bond layer surrounding the metal blade core. The circles numbered 1-9 mark locations of thermocouples.

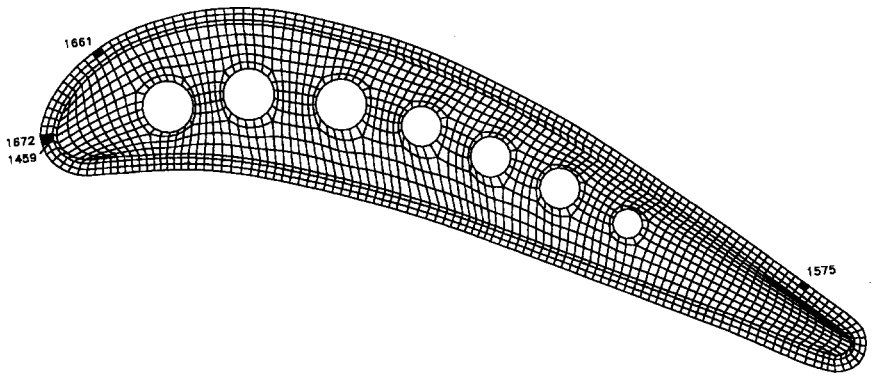

Fig. 5 Discretized cross-section of the turbine blade. The outer two element layers represent the ceramic coating. Numbered elements are referred to later in the text.

Table 1 Summary of thermal and mechanical material properties for coated blade

Property	Blade core	Bond layer	Ceramic coating
E[GPa]	205-120	172-3.5	20
ν	0.3	0.3	0.15
$\alpha[10^{-6}$ l/K]	12.9-19.2	12.5-19.2	11
λ[W/Km]	11.5-35.7	11.5-35.7	0.95-1.11

Modulus of elasticity E
Poisson's ratio ν
Coefficient of linear thermal expansion α
Thermal conducitivy λ

the 0.3 mm ceramic coating (ZrO_2 with 7 weight % Y_2O_3). Most of the thermal and mechanical material properties vary nonlinearly with temperature. The range of variation within the tempera-

ture interval in question (200℃-1200℃) is indicated in Table 1 . For a complete documentation comprising mathematical expressions and diagrams along with a reference to the sources for the respective data see (Modelcoat 1994).

The thermal stress analysis requires apart from the initial conditions the input of the transient temperature field in the blade during cycling. The latter may be determined by the numerical solution of a non-stationary thermal problem for the turbine blade subjected to the external flow of hot or cool gas, and the cooling air flowing through the interior holes. The model relies on the heat transfer coefficients at the internal and external boundaries of the blade which are usually missing. The present investigations base therefore the determination of transient temperature fields entirely on data measured along the contour of the profile. In modelling coating production and the cycling test, the thermal strains constitute the only loading. Under more general service conditions additional loads may be imposed to the finite element model as a consequence of aerodynamic forces and inertia, for instance.

The completion of the thermomechanical analysis requires modelling of the deterioration of the elastic properties in the ceramic coating because of microcracking. To this purpose, the software module developed for micromechanics investigations was adapted to the FEPS software and may be activated during the course of the finite element stress analysis of the macroscopic component. The interaction between microstructure and finite element algorithm is as follows. At each instant during stress analysis, the elastic strains determined at critical locations in the finite element model are communicated to the micromechanics module and are imposed to the local structure. The module then examines a possible formation of microcracks, updates the microcrack pattern and returns the modified elastic properties and the appertaining stress state to the finite element algorithm. The next time instant can be usually addressed already after two equilibrium iterations, ruling the disturbance of the linearity caused by the material damage, cf. Eq. (6). The above completely interactive scheme coupling the continuum level to the microstructure model, is certainly unavoidable when the state of strain varies widely within the ceramic coating, and/or the strain components at critical locations do not vary in proportion to each other, at least approximately.

The case of the turbine blade investigated here under plane stress conditions is, however, characterized by the appearance of a simple state of strain in the ceramic coating. The circumferential strain is the predominant component, and is accompanied by the ordinary elastic contractions. Smaller radial strain components appear in the curved regions of the profile, shear strains may be considered absent. At each location in the coating, the strain components may be seen to vary proportional to each other during thermal cycling. Since the strain mode remains fixed, the response of the ceramic microstructure to the imposed straining may be investigated a priori and provides a stress-strain law for the damaging material appertaining to the particular location under consideration. The microstructural model supplies the stress state and the elastic properties as a function of the intensity of the imposed strain along with the microcrack pattern. This is exemplified in Fig. 2 and Fig. 3. Our studies suggest that within the range of variation of the essentially biaxial strain mode in the coating of the blade, the damaging behaviour of the ceramic material may be considered unique. In the finite element algorithm, the elastic strain obtained at each instant is now communicated to the already modelled response of the damaging material instead to activating the micromechanics module. The associated local state of stress and the elastic properties are returned to the finite element procedure by the pre-determined material law. A continuing reduction of the elastic properties is associated with the deterioration

of the microstructure due to increasing straining. Unloading is assumed to leave the - possibly reduced - elastic parameters unaffected.

Upon appearance of localization patterns a macroscopic crack is considered, and its potential to extend is studied by fracture mechanics analysis. In this connection the fracture mechanics module of the finite element program system ASKA could be employed (Doltsinis, *et al.* 1979) as extended here to the presence of thermal loading. For fracture mechanics investigations, segments of the coating are modelled separately and are subject to the transient loading conditions resulting from the complete finite element model of the cross-section of the turbine blade.

6. Manufacturing of coating

Residual stresses arising from the application of the coating on the turbine blade are determined for spraying performed under controlled conditions in the factory. The blade, supplied with the bond layer, is subjected to the process of the deposition of the ceramic material by plasma spraying which induces elevated temperatures in the material. Cooling is effected by air through the internal hole system in the blade. When the molten droplets of ceramic material splat on the substrate, they cool rapidly down from over 3000 K to less than 1000 K, and are subject to quenching stresses resulting from hindered thermal contraction. After completion of the spraying process, the assembly of component and coating is cooled-down to ambient temperature and causes additional stresses because of different thermal expansion coefficients and/or the non-homogeneous temperature distribution at deposition.

During the production of the coating, the temperatures were measured at a cross-section by thermocouples positioned along the periphery of the original blade profile, cf. Fig. 4, and were recorded at several instants. Fig. 6 reproduces the time history of the temperature at four representative locations exhibiting highest (~450℃) and lowest values (~150℃) along the periphery of the core material of the blade. Oscillations in the temperature indicate the passage of the point considered through the plasma jet depositing the ceramic material. The plasma jet is moving periodically, whilst the blade is subject to a rotation about its longitudinal axis such

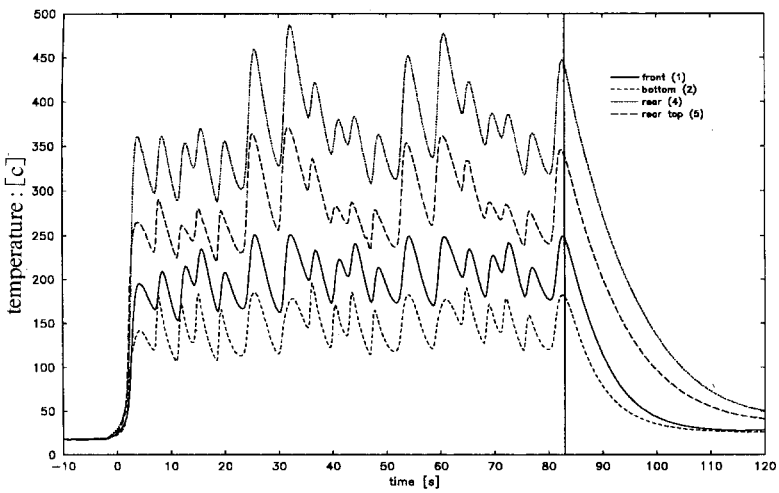

Fig. 6 Temperature variation during spraying at the locations of some thermocouples. The vertical line marks the instant when cooling-down is considered to commence (83 sec).

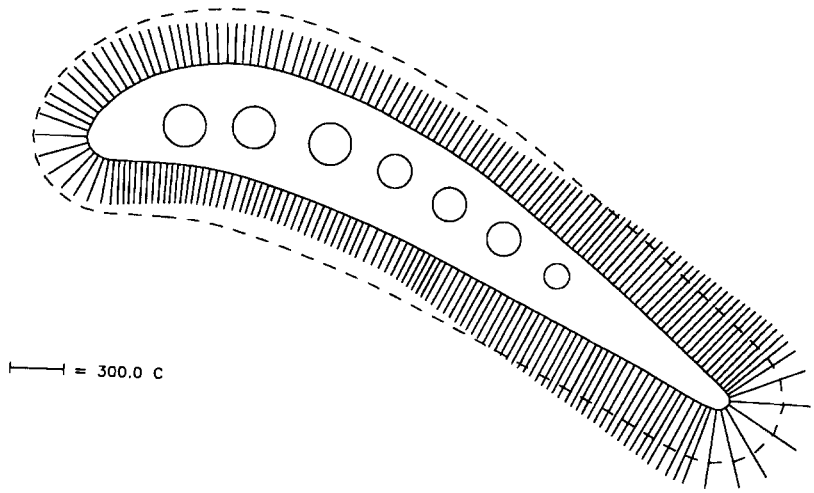

Fig. 7 Temperature along the periphery of the blade obtained by linearly interpolating between the thermocouple locations.

that the entire surface is consecutively exposed to the deposition of the coating material. After completion, the coated blade is cooled-down to ambient temperature. With reference to Fig. 6, the cooling-down phase may be considered starting after approximately 83 seconds.

The model for the computation of the residual stress considers the ceramic coating to behave as a compact elastic material only after complete deposition. That means that local thermomechanical processes evolving during spraying are not considered in detail, but are merely reflected by the resulting microstructure and the elastic properties of the coating material after deposition ($E=20$ GPa). The residual stresses are obtained as a consequence of the cooling-down to ambient temperature (30℃) of the coated component as from the temperature at the end of the spraying. It is assumed that core material and bond layer are stress-free at 30℃ and develop thermal strains with reference to this temperature. For the coating, the stress-free state is taken at the end of the spraying.

The temperature distribution in the cross-section of the blade at the end of the spraying, after approximately 83 seconds is determined as follows. The temperatures measured at nine positions by thermocouples, are used as pivot values for an interpolation furnishing the temperature distribution along the periphery of the cross-section underneath the bond layer, Fig. 7. This, supplemented by an estimation of the temperature at the boundaries of the internal cooling holes in the blade, specifies a finite element computation of the temperature variation in the interior of the core material for prescribed boundary values.The temperature field in the cross-section as resulting from the computation is visualized in Fig. 8. The figure indicates also the temperature variation in the bond layer and the ceramic coating. To this purpose, the temperature gradients across the layers were deduced from that determined in the core material, assuming an inverse proportionality to the thermal conductivity of the individual materials. Accordingly, the temperature gradient in the core near the boundary extends unaltered over the bond layer, whilst it is magnified by a factor of 15 in the ceramic layer.

Cooling-down from the thermal state at the end of spraying to the homogeneous ambient temperature of 30℃ leaves stresses in the cross-section of the coated component which are determined by a finite element computation.

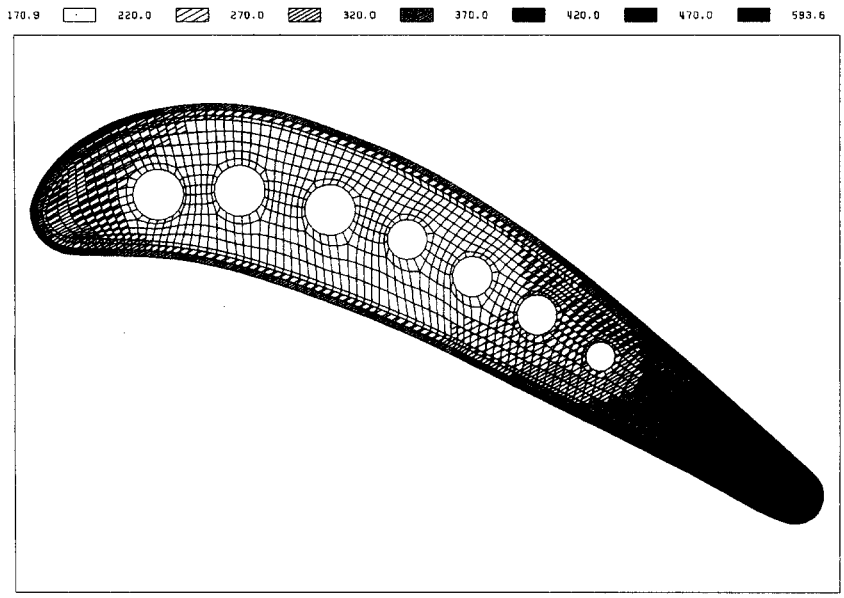

Fig. 8 Temperature distribution in the cross-section of the coated blade after spraying (values in °C).

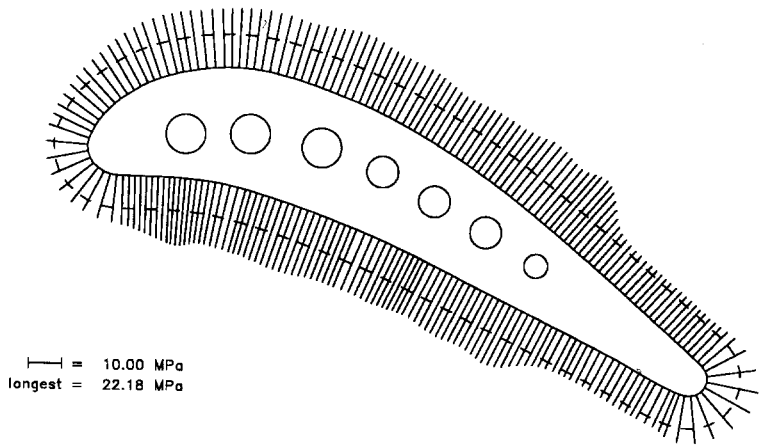

Fig. 9 Circumferential manufacturing stresses in the middle of the thermal barrier coating. The dashed line marks the value of 10 MPa.

Fig. 9 shows, as a numerical result, the variation along the periphery of the circumferential stress component in the middle of the ceramic layer. This stress is tensile in nature and its intensity ranges to approximately 20 MPa, the elastic strain is in the order of 10^{-3}. Higher stresses, appearing on the outer surface of the coating are up to 35 MPa and within the range of laboratory measurements. The results from micromechanical studies, Fig. 3, suggest that under these conditions the material does not exhibit any appreciable damage by microcracking. Radial stresses appear in the coating merely at the regions of pronounced curvature of the profile, i.e., at the leading and the trailing edge. They are compressive in nature and about four times lower in their maximum intensity than the circumferential component.

The strong dependence of the thermomechanical properties of core material and bond layer

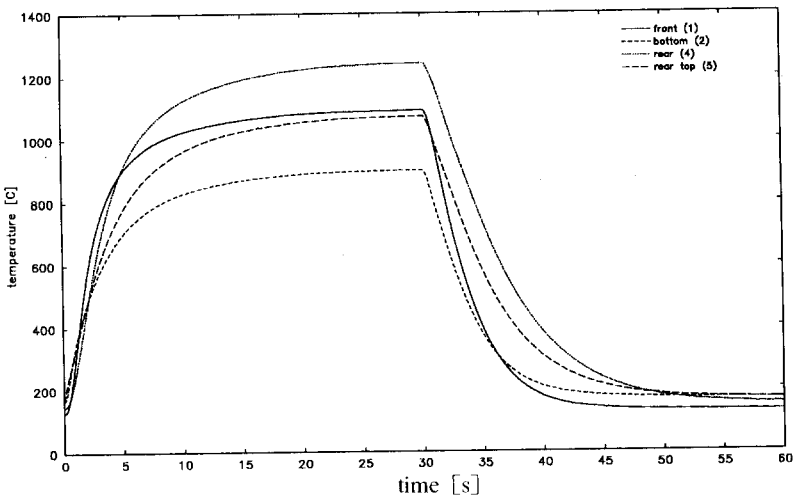

Fig. 10 Temperatures at the locations of some thermocouples during cycling for the reference test.

has a decisive influence on the mode of interaction between the mechanical state left in the coated blade and the transient stresses during thermal cycling. Since the temperature in the core is raised then up to ≈1200℃, the residual stresses are not simply superimposed to those appearing in the coating during thermal cycling.

7. Thermal cycling of the coated component

The computer simulation of thermal cycling refers to tests on the coated turbine blade, performed by the manufacturer. The test conditions are characterized by the temperature of the external heating gas and the pressure of the internal cooling air. The thermal cycles consist of a heating phase of 30 seconds which is followed by a cooling period of another 30 seconds.

The instrumentation of the tests was as in the production of the coating, cf. Fig. 4. A graphical representation of the temporal variation of the temperature at four from the nine thermocouple locations is provided in Fig. 10 for a single cycle indicating the intervals of heating and cooling. The data are from the single test in the series, characterized by a heating gas temperature of 1485℃ and a pressure of the internal cooling air of 3950 hPa. This test was selected as a reference case for the numerical analysis because it allowed utilization of previous numerical results in specifying the thermal conditions in conjunction with the measured data.

To be specific, interpolation of the values measured along the profile, combined with computed temperatures at the cooling holes provided the boundary conditions for the determination of the temperature field in the core of the blade. Referring to Eq. (8), only a stationary problem has to be solved for prescribed temperature values. Thereby, thermomechanical coupling associated with the time rates, Eq. (14), becomes irrelevant. In addition, the measured values were extrapolated across the bond layer and the ceramic coating as based on temperature gradients obtained previously by the finite element model. This completes the calculation of the temperature distribution at several instants during the heating and the cooling phase. The mechanical response of the turbine blade to the thermal action, computed at the same instants in the cross-section under investigation, gives a transient impression of the strains and stresses appearing there.

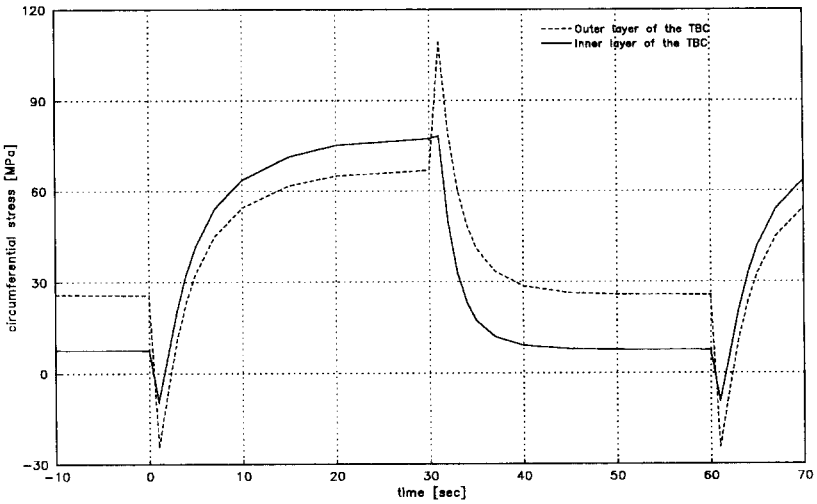

Fig. 11 Circumferential stress-time diagram over one heating/cooling cycle at the leading edge. Comparison between the stress in the outer layer (element no. 1672, dashed line) and the inner layer (element no. 1459, solid line) of the ceramic TBC (no damage).

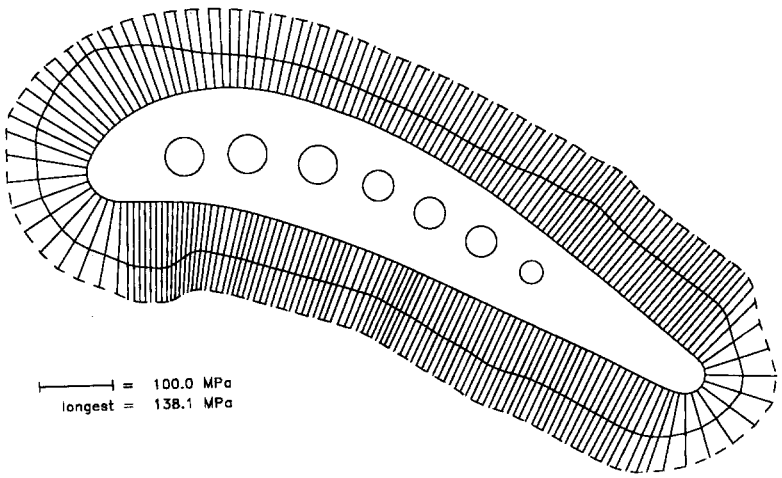

Fig. 12 Circumferential stresses at the instants $t=30$ sec (solid) and $t=31$ sec (dashed) in the outer element layer for the undamaged ceramic TBC.

The region of our particular interest is the ceramic coating where the circumferential stress is the predominant component. The highest values appear in the outer element layer of the coating, cf. Fig. 5, with a maximum value on the suction side in element no. 1575 located at the rear part of the profile. The variation of the circumferential stress during the thermal cycle is depicted in Fig. 11 for a position at the leading edge. In the figure, the dashed line refers to the outer element layer of the coating (element no. 1672), the solid line to the inner layer (element no. 1459) at the same peripheral position. The results reflect the time history of the stress as obtained by a finite element simulation which ignores the occurrence of damage in the ceramic material. The peak values of the stress in Fig. 11 at $t=31$ sec are a consequence

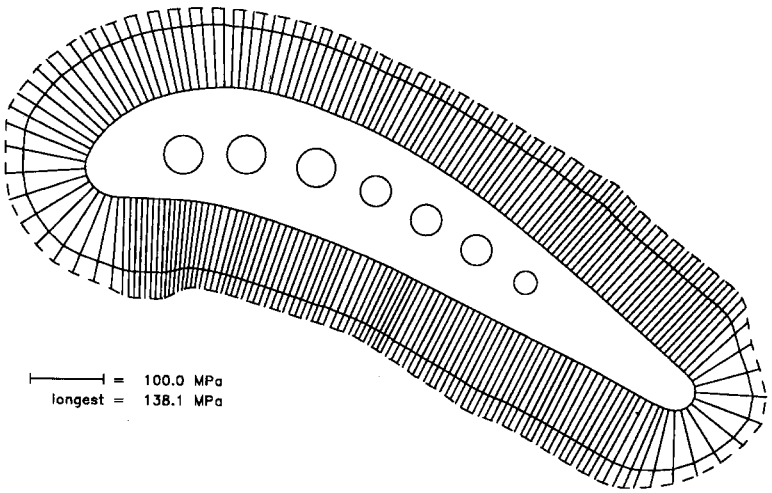

Fig. 13 Comparison of circumferential stresses in the outer element layer of the ceramic TBC at $t=31$ sec with (solid) and without considering microstructural damaging (dashed).

of the sudden changes in outside temperature from 1485℃ to 50℃ at the end of the heating phase, which acts as a cooling shock in the outer fibers of the coating but does not affect interior regions. A similar phenomenon occurs at the transition from cooling to heating. The distribution of the circumferential stress in the coating along the periphery at the end of the heating-up phase at $t=30$ sec and after the onset of cooling down, at $t=31$ sec is depicted in Fig. 12 for the outer element layer of the TBC. It is seen how the thermal contraction of the ceramic layer alters the distribution.

Whilst discussion of the above results demonstrates the significance of the operation conditions for an elastic coating, though temperature dependent response of core material and bond layer, an alternative simulation accounts for the damaging of the ceramic coating as well. It yields results which are characterized by a substantial reduction of the stress intensity. Damage is accounted for in the ceramic coating in accordance with the material model of Fig. 3 resulting from micromechanics analysis. The maximum circumferential elastic strain in the thermal cycle amounts to 7×10^{-3}, corresponding to a stress of 140 MPa in the undamaged material with an elastic modulus of 20 GPa. Damage reduces up to this strain the elastic modulus to 13.5 GPa thus inducing a stress of only 95 MPa. Fig. 13 shows the distribution of the circumferential stress component along the profile for the outer element layer of the ceramic coating at $t=31$ seconds. It also demonstrates how damage of the microstructure reduces the stress as compared to the non-damaging case.

8. Analysis of failure

For a discussion on the probability of failure we consider the computed stress distribution in the coating at $t=31$ sec in Fig. 13. Reference to the topology of Fig. 5 may help to identifying critical locations. It may be seen from Fig. 13 that at this stage where the largest stresses appear, the coating has undergone damage by microcracking entirely over the periphery of the cross-

section.

At the rear part on the profile, circumferential tensile elastic strains and consequently stresses are highest in the region between the last cooling hole and the beginning of the curvature of the trailing edge. At a first sight, the conditions there appear to be the same on the pressure and the suction side. On both sides the stress, essentially constant, exhibits a weak local maximum just behind the last cooling hole as well as at the transition to the curved part of the trailing edge. At the latter location the elastic strain and the stresses assume the highest values before they decrease considerably over the trailing edge. This result conforms with the failure patterns observed in the coating after a few cycles. Photographs of magnified images indicate indeed cracking across the coating on both the pressure and the suction side at the computed stress maximum behind the last cooling hole and at the transition of curvature at the trailing edge. Cracking across the coating is observed also in the middle between the maxima where the flat stress profile maintains the high intensity. Although at this early stage we may rather speak of fissures across the coating, in the main, two open segmentation cracks appear each on either side of the tail. On the pressure side, the segmentation crack is definitely located at the curvature transition, whilst on the suction side, segmentation may alternatively occur at the middle location with a fissure then visible at the rear stress maximum. Ultimately, segments of the coating are detached from the profile around the trailing edge.

At the nose region of the profile, higher stresses appear in the ceramic coating as from underneath the first cooling hole up to the location of element no. 1661, Fig. 5. Their maximum value on the pressure side is the same as at the tail. Stresses are somewhat lower on the upper side of the nose. Although this is true at the instant of $t=31$ sec, up to this time the maximum circumferential stress in the coating appears on the upper side, at the location of element no. 1661, cf. Fig. 5. Here, a fissure is visible across the ceramic coating at early stages of the cycling test. At $t=31$ sec this maximum moves locally down to slightly above the leading edge, element no. 1672. In the tests, failure of the coating occurs on the upper side of the nose after a high number of thermal cycles. Despite the higher stresses, failure does not occur at the single concave region on the pressure side.

The above considerations may suggest the following two stages of modelling failure of the coating. First, the material undergoes damage by distributed microcracking as accounted for by the micromechanics approach. Depending on the local structure in the coating, microcracks

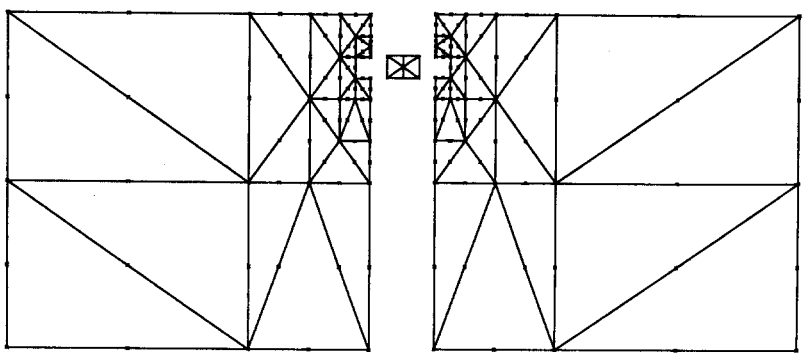

Fig. 14 Segment of the ceramic TBC. FE-modelling of a crack emanating from the outer surface (suction side).

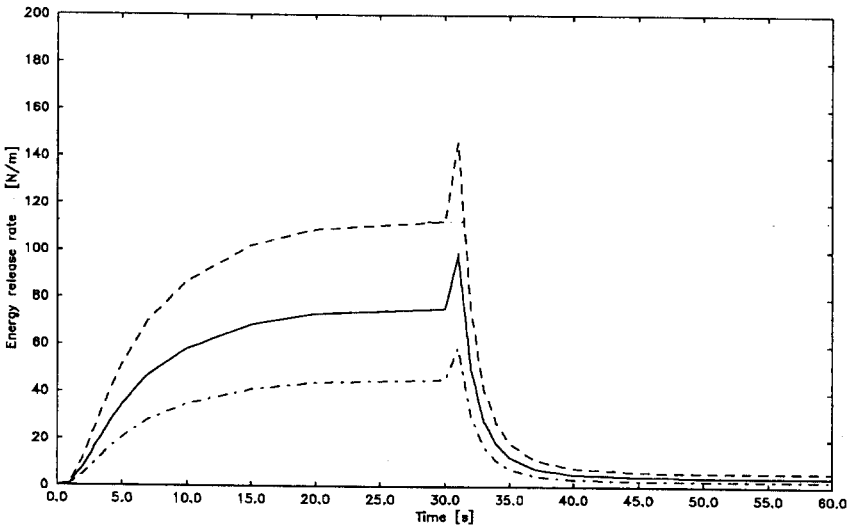

Fig. 15 Variation of energy release rate during thermal cycle (suction side, leading edge) Crack 47 μm, $E=20$ GPa./Crack47 μm, $E=13.7$ GPa./Crack 28 μm, $E=13.7$ GPa.

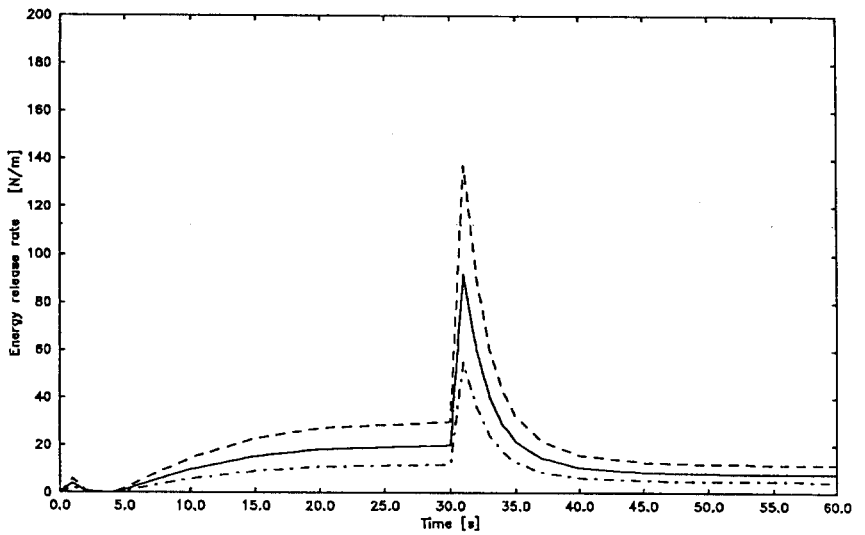

Fig. 16 Variation of energy release rate during thermal cycle (suction side, trailing edge) Crack 47 μm, $E=20$ GPa./Crack47 μm, $E=13.7$ GPa./Crack 28 μm, $E=13.7$ GPa.

may accumulate to form distinct macroscopic crack patterns as from a certain strain level, cf. Fig. 2. The extension of macroscopic cracks and the estimation of critical crack lengths is then based on fracture mechanics investigations accounting for the deterioration of the material properties due to preceeding material damage. Whilst microstructure damage was accounted for entirely in the coating for the stress analysis of the cycling tests, for fracture mechanics investigations we selected the locations of element nos. 1661 and 1575, cf. Fig. 5. To this purpose, segments of the ceramic coating are discretized separately with a crack introduced normal to the periphery emanating from the outer surface, Fig. 14. Use of triangular elements with 6 nodes allows model-

ling of the crack tip singularity (Barsoum 1976).

The segment is subjected to the transient thermal loading from the cycling test in its interior and to displacements imposed on its boundaries as computed by the complete finite element model. The variation of the energy release rate during the thermal cycle for the crack at the nose is represented in Fig. 15. The upper curve appertains to an assumed crack of 47 μm introduced in the undamaged material ($E=20.0$ GPa). The middle curve (solid line) demonstrates the effect of material damage ($E=13.7$ GPa) for the same crack length, whilst the lower curve refers to a shorter crack of 28 μm in the damaged material. Similarly, Fig. 16 documents the result of the fracture mechanics investigation at the tail of the profile. In both cases the energy release rate increases smoothly during the heating phase and is succeeded by a sudden increase of the instants following the transition to the cooling phase. This effect is more pronounced at the rear location. We also investigated crack propagation at the location of maximum stress on the pressure side of the nose region, cf. Fig. 13. The energy release rate varies as at the rear location, Fig. 16, the values here being more than 20% lower.

Since at the tail segmentation cracks appear within the first few cycles, we may conclude that intense straining indeed induces localized microcrack patterns here which propagate as macroscopic cracks across the thickness. At the nose, although the upper location of high strain, on the suction side, is most prone to macroscopic crack extension, material damage is less intense and distinct cracks are formed in the test after a large number of thermal cycles and propagate then. The location of the maximum strain on the pressure side, is exposed to highest straining, but is by far less prone to macroscopic crack propagation. In addition, it may be assumed that the microstructure of the coating at this concave region favours rather the formation of distributed microcracking networks than of localized patterns. As a result, macroscopic failure is not detected here.

9. Conclusions

A methodology was presented for the numerical modelling of the manufacturing process for the application of ceramic thermal barrier coatings, and of thermal cycling of coated turbine blades. The proposed technique combines finite element analysis on the continuum level with the micromechanics of damage on the structural level of the ceramic material. The study aims particularly at an assessment of failure of the coating under service conditions.

Our concept of failure starts with the damage of the coating material by distributed microcracking in the ceramic. This may be succeeded by the formation of macroscopic crack patterns as a result of localization above certain strain levels. The macroscopic cracks can finally assume critical lengths and propagate across the entire thickness of the ceramic layer, thus leading to segmentation of the coating. Analysis of tested turbine blades supports the idea that damage and failure are not necessarily the result of accumulative processes during thermal cycling, but occur rather spontaneously at early stages of the test. The potential for macroscopic crack extension can be diminished by the admission of distributed microcracking in the ceramic material, on the one hand, and by preventing the formation of macroscopic crack patterns on the other hand. Thus, although a certain amount of straining is desirable in order to induce damage of the microstructure, it has to be maintained below the localization level.

Acknowledgements

The experimental data were supplied by Dr. Thomas Cosack, MTU-Munich. The present work was financially supported by the BRITE/EURAM programme of the Commission of the European Union (Brite/Euram Project BE-4272-90, Modelcoat).

References

Barsoum, R.S. (1976), "On the use of isoparametric finite elements in linear fracture mechanics", *Int. J. Num. Meth. Engng.*, **10**, 25-37.

Buresch, F.E. (1985), "Relations between the damage in and microstructure of ceramics", *Materials Science and Engineering*, **71**, 187-194.

Davidge, R.W., Mc Laren, J.R. and Titchell, I. (1983), "Statistical aspects of grain boundary cracking in ceramics and rocks", *Fracture Mechanics of Ceramics*, **5**, 495-506.

Doltsinis, I.St., Eggers, M. and Handel, R. (1992), "Properties of thin ceramic layers", in Modelling and characterization of the manufacturing process of ceramic thermal barrier coating, BRITE/ EURAM Project BE-4212-90, 1st Progress Report, ICA-Stuttgart.

Doltsinis, I.St. (1993), "Coupled field problems - Solution techniques for sequential and parallel processing", in *Solving Large-Scale Problems in Mechanics*, edited by M. Papadrakakis, Wiley.

Doltsinis, I.St. (1979), "Zur Berechnung des Rissvortschritts in inelastischen Tragwerken", *ZAMP*, **30**, 57-64.

Doltsinis, I.St., Eggers, M., Haller, K.-U. and Handel, R. (1995), "Finite element modelling of ceramic thermal barrier coatings to extend the operating range of heat engine components", BRITE/EURAM Project BE-4272-90, 6th Progress Report, ICA-Stuttgart.

Doltsinis, I.St. (1990), "Aspects of modelling and computation in the analysis of metal forming", *Engineering Computations*, 7, 2-20.

Doltsinis, I.St., Knapp, H., Streiner, P. and Wüstenberg, H. (1979), "ASKA-FM, fracture mechanics", *ASKA UM* 226, ISD-Stuttgart.

Kachanov, M. (1992), "Effective elastic properties of cracked solids: critical review of some basic concepts", in *Micromechanical Modelling of Quasi-brittle Behaviour;* edited by V.C.L. Li, Appl. Mech. Rev., **45**, 304-335.

Kachanov, M. (1987), "Elastic solids with many cracks: A simple method of analysis", *Int. J. Solids and Structures*, **23**, 23-43.

Modelcoat (1994), "Finite element modelling of ceramic thermal barrier coatings to extend the operative range of heat engine components" BRITE/EURA7 Project BE-4272-90, 4th Progress Report, ICA-Stuttgart.

Wüstenberg, H. (1986), "FEPS 3.3. Finite Element Programming System: User's Guide", *ICA Report* 21, and "FEPS 3.3.: Element Library", *ICA Report* No. 22, Stuttgart. User's

Zaat, J.H. (1983), "A quarter of century of plasma spraying", *Annual Review of Material Science*, **13**, 9-42.